

Original citation:

Reith, Lukas, Lienau, Karla, Cook, Daniel Sean, Moré, René, Walton, Richard I. and Patzke, Greta Ricarda (2018) *Monitoring the hydrothermal growth of cobalt spinel water oxidation catalysts - from preparative history to catalytic activity*. Chemistry - A European Journal. doi:[10.1002/chem.201801565](https://doi.org/10.1002/chem.201801565)

Permanent WRAP URL:

<http://wrap.warwick.ac.uk/102725>

Copyright and reuse:

The Warwick Research Archive Portal (WRAP) makes this work by researchers of the University of Warwick available open access under the following conditions. Copyright © and all moral rights to the version of the paper presented here belong to the individual author(s) and/or other copyright owners. To the extent reasonable and practicable the material made available in WRAP has been checked for eligibility before being made available.

Copies of full items can be used for personal research or study, educational, or not-for profit purposes without prior permission or charge. Provided that the authors, title and full bibliographic details are credited, a hyperlink and/or URL is given for the original metadata page and the content is not changed in any way.

Publisher's statement:

"This is the peer reviewed version of the Reith, Lukas, Lienau, Karla, Cook, Daniel Sean, Moré, René, Walton, Richard I. and Patzke, Greta Ricarda (2018) *Monitoring the hydrothermal growth of cobalt spinel water oxidation catalysts - from preparative history to catalytic activity*. Chemistry - A European Journal. which has been published in final form <https://doi.org/10.1002/chem.201801565>

This article may be used for non-commercial purposes in accordance with [Wiley Terms and Conditions for Self-Archiving](#)."

A note on versions:

The version presented here may differ from the published version or, version of record, if you wish to cite this item you are advised to consult the publisher's version. Please see the 'permanent WRAP URL' above for details on accessing the published version and note that access may require a subscription.

For more information, please contact the WRAP Team at: wrap@warwick.ac.uk

CHEMISTRY

A European Journal

A Journal of



Accepted Article

Title: Monitoring the hydrothermal growth of cobalt spinel water oxidation catalysts - From preparative history to catalytic activity

Authors: Lukas Reith, Karla Lienau, Daniel S. Cook, René Moré, Richard I. Walton, and Greta Ricarda Patzke

This manuscript has been accepted after peer review and appears as an Accepted Article online prior to editing, proofing, and formal publication of the final Version of Record (VoR). This work is currently citable by using the Digital Object Identifier (DOI) given below. The VoR will be published online in Early View as soon as possible and may be different to this Accepted Article as a result of editing. Readers should obtain the VoR from the journal website shown below when it is published to ensure accuracy of information. The authors are responsible for the content of this Accepted Article.

To be cited as: *Chem. Eur. J.* 10.1002/chem.201801565

Link to VoR: <http://dx.doi.org/10.1002/chem.201801565>

Supported by
ACES

WILEY-VCH

FULL PAPER

Monitoring the hydrothermal growth of cobalt spinel water oxidation catalysts - From preparative history to catalytic activity

Lukas Reith,^[a] Karla Lienau,^[a] Daniel S. Cook,^[b] René Moré,^[a] Richard I. Walton,^[b] and Greta R. Patzke^{*[a]}

Abstract: The hydrothermal growth of cobalt oxide spinel (Co_3O_4) nanocrystals from cobalt acetate precursors was monitored with in situ powder X-ray diffraction (PXRD) in combination with ex situ electron microscopy and vibrational spectroscopy. Kinetic data from in situ PXRD monitoring were analyzed using *Sharp-Hancock* and *Gualtieri* approaches, which both clearly indicate a change of the growth mechanism for reaction temperatures above 185°C. This mechanistic transition goes hand in hand with morphology changes that notably influence the photocatalytic oxygen evolution activity. Complementary quenching investigations of conventional hydrothermal Co_3O_4 growth demonstrate that these insights derived from in situ PXRD data provide valuable synthetic guidelines for water oxidation catalyst production. Furthermore, the ex situ analyses of hydrothermal quenching experiments were essential to assess the influence of amorphous cobalt-containing phases arising from the acetate precursor on the catalytic activity. Thereby, we illustrate how the efficient combination of a single in situ technique with ex situ analyses paves the way to optimize parameter-sensitive hydrothermal production processes of key energy materials.

Introduction

Artificial photosynthesis is a central strategy for the conversion of solar energy into chemical fuels.^[1] The main challenge of the water splitting reaction is the four electron transfer process required for the oxidation half reaction of water to oxygen. The development of efficient, stable, and economic water oxidation catalysts (WOCs) has thus become a forefront current research field.^[2,3] Spinel-type Co_3O_4 attracts strong research interest as a low-cost and robust alternative to expensive Ru, Ir, and Pt-containing WOCs.^[4] Moreover, Co_3O_4 is a key material with a broad range of applications, such as in sensors,^[5,6] battery electrodes,^[7] data storage,^[8] general heterogeneous catalysis,^[9,10] and many other areas. However, exerting full control over the various performance parameters of cobalt oxides, namely particle/crystallite size,^[11] crystallinity,^[12] oxidation states,^[13]

crystal structure,^[14] defects,^[15] morphology,^[16,17] and surface area^[18] remains a preparative and analytical challenge. Therefore, a wide range of synthetic routes to nanostructured spinel-type cobalt oxide has been investigated.^[19]

Among them, hydro/solvothermal methods offer particularly attractive access to tunable nanosized Co_3O_4 materials^[20] due to their widely adjustable parameter space. In principle, optimization of hydro/solvothermal precursors, oxidants, solvents, surfactants, additives, temperatures, or reaction times, holds the key to controlling all of the above-mentioned performance parameters of nanoscale oxide WOCs.^[21,22,23] However, to fully explore this design potential, further mechanistic studies are now required to enlighten the mainly empirical “black box” nature of hydro/solvothermal methods.

To this end, time-resolved XRD experiments can provide direct insight into the mechanism of hydrothermal reactions.^[24–27] Such synchrotron-based techniques have been applied to study growth and crystallization of different material types, such as zeolites,^[28] metal organic frameworks (MOFs),^[29–31] polyoxometalates (POMs),^[32] and metal oxides.^[25,26] The elucidation of growth mechanisms through time-dependent XRD measurements paves the way to targeted hydrothermal parameter optimization for accessing selective materials' properties. This strategy is applicable for nanostructured materials in principle and now remains to be explored to track the growth of key WOC types.^[26,33] We here present new insights into the growth process of nanoscale Co_3O_4 WOCs using the Oxford-Diamond in situ cell (ODISC) as a powerful tool for performing time-resolved XRD experiments.^[34] This setup on beamline I12 at the Diamond Light Source, UK,^[35] provides sufficient X-ray energy to study hydrothermal reactions in a realistic lab-scale setup using a PTFE-lined steel autoclave. Our previous work involving the ODISC, for example, revealed the presence of intermediate layered double hydroxides phase during the solvothermal growth of CoGa_2O_4 .^[25]

The proven strong dependence of the catalytic activity of Co_3O_4 WOCs on the materials' parameters^[10,17,23,36] renders it an ideal target to control them by synthesis through insight into the underlying growth mechanisms. We thus compare results from time-resolved XRD monitoring of hydrothermal Co_3O_4 growth using the ODISC setup with trends of analogous quenching experiments. Furthermore, the photocatalytic performance of Co_3O_4 samples prepared during the in situ experiments and those synthesized conventionally is compared. This comprehensive study connects the growth kinetics of Co_3O_4 with the resulting materials properties to bring forward essential correlations between the preparative history of Co_3O_4 and its catalytic performance.

[a] L. Reith, K. Lienau, Dr. R. Moré, Prof. Dr. G. R. Patzke
Department of Chemistry
University of Zurich
Winterthurerstrasse 190, CH-8057 Zurich, Switzerland
E-mail: greta.patzke@chem.uzh.ch

[b] D. S. Cook, Prof. R. I. Walton
Department of Chemistry
University of Warwick
Coventry CV4 7AL, United Kingdom

Supporting information for this article is given via a link at the end of the document.

FULL PAPER

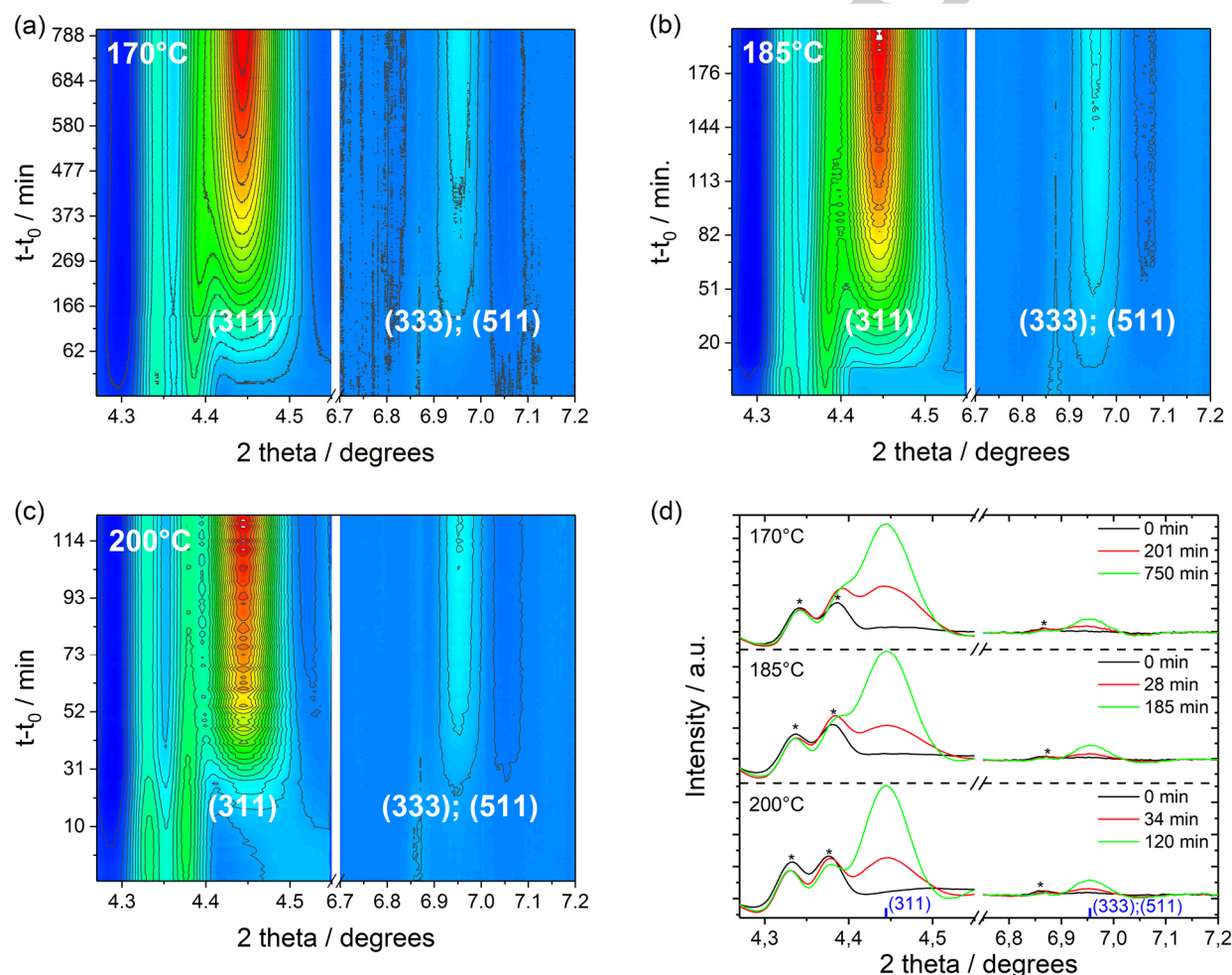


Figure 1. (a-c) Visualization of time-resolved XRD patterns in a contour-plot for different temperatures ($\lambda = 0.18893 \text{ \AA}$, intensity increases in the order blue-green-yellow-red); (d) Bragg reflections of Co_3O_4 for different reaction times (* = reflection of the partial crystalline PTFE liner, blue bars = positions of the (311), (333), and (511) reflections, respectively).

Results and Discussion

Time resolved PXRD monitoring of Co_3O_4 formation. In all time-resolved experiments, the PXRD patterns show Bragg reflections prior to heating, which arise from the stainless steel autoclave and from the partially crystalline PTFE liner. After an induction time (t_0), the emerging new Bragg reflections were all assigned to the Co_3O_4 phase and no evidence for any crystalline intermediate was found. Within the measurement window, the intensities of the most pronounced (311) reflection (see Figure 1) were determined by peak fitting.

The extent of reaction α was determined from the relative intensity of the (311) reflection after background subtraction. The temporal evolution of α shows a very slight sigmoidal growth at 170°C and 185°C , on the verge of monoexponential. In contrast, the growth behavior at 200°C is clearly sigmoidal (Figure S3). Table S1 summarizes the mathematical expressions for different growth models^[37,38] which are divided into four groups, namely diffusion controlled growth (D_1 - D_4), phase-boundary controlled growth (R_2 and R_3), first order growth model (F_1), and nucleation & growth

model (A_2 - A_4). A plot of the extent of reaction α vs. $t-t_0/t_{1/2}$ is compared to these different growth models in Figure 2. At 170°C , the reaction fits well with the phase boundary model R_3 . The formation of Co_3O_4 at 185°C can best be described with the first-order model F_1 . Finally, the comparison of the experimental data recorded at 200°C with different growth models suggests a clear change towards Johnson Mehl Avrami Kolmogorov (JMAK) growth kinetics A_2 .

The experimental data was further analyzed on the basis of the JMAK model according to eq. 1.^[39]

$$\alpha = 1 - e^{-(k(t-t_0))^n} \quad (\text{eq. 1})$$

Here, the JMAK model was used in its linearized form, also known as a *Sharp-Hancock* plot, where the *Avrami* parameter n can be determined from the slope of a plot of $\ln(-\ln(1-\alpha))$ vs $\ln k$ (eq. 2).^[37]

$$\ln(-\ln(1-\alpha)) = n \cdot \ln k + n \cdot \ln(t-t_0) \quad (\text{eq. 2})$$

The *Sharp-Hancock* plots for the experimental data recorded at 170°C and 185°C , respectively, display very closely related slopes (n) of 1.20 ± 0.01 and 1.07 ± 0.01 .

FULL PAPER

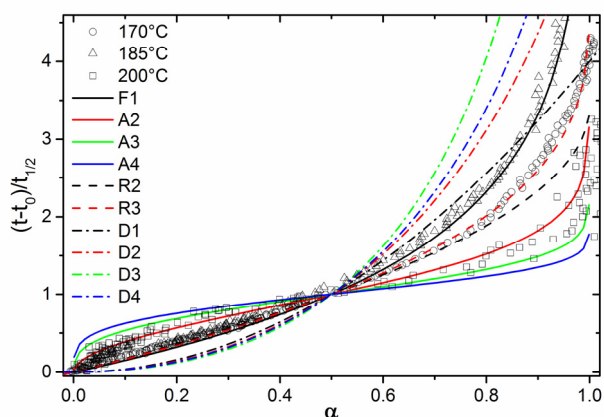


Figure 2. Plot of the extent of the reaction α vs $t-t_0/t_{1/2}$ compared with different growth models (cf. Table S1 for details).

Therefore, it is safe to assume that a similar growth mechanism takes place at these reaction temperatures. In sharp contrast, the *Sharp-Hancock* plot for Co_3O_4 formation at 200 °C results in a higher slope of 2.37 ± 0.07 . This clearly points to a change in the reaction mechanism when the reaction temperature is raised above 185 °C (see Figure 3).

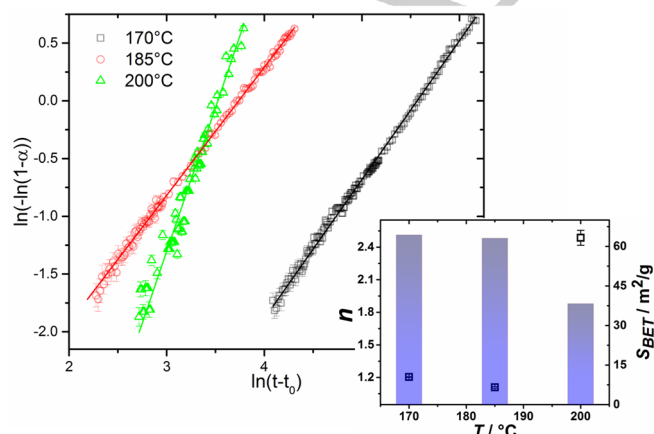


Figure 3. *Sharp-Hancock* plots for the growth of the (311) Bragg reflection of Co_3O_4 at different temperatures over the range $0.15 < \alpha < 0.85$. Inset: Temperature dependence of the *Avrami* coefficient n (black squares) and correlation with the specific surface area of samples obtained after the in situ experiments (blue bars).

The temperature dependence of the rate of Co_3O_4 formation does not show a typical linear behavior in the Arrhenius plot (Figure S1). This is in line with the change of growth mechanism between 185 °C and 200 °C. However, keeping in mind that the widely applied JMAK approach was originally developed as a model for solid-state reactions in alloys, we next applied the alternative *Gualtieri* approach for the analysis of hydrothermal crystallizations that was implemented for zeolites, MOFs or POMs.^[28–30,32] This approach describes solution mediated reactions with separate nucleation and crystallization steps (eq. 3).

$$\alpha = \frac{1}{1 + e^{-(t-a)/b}} (1 - e^{-(k_g t)^n}) \quad (\text{eq. 3})$$

The first term of this equation describes the nucleation (a = maximum nucleation rate, b = distribution of the nucleation probability). The parameters a and b define the probability of nucleation P_N (eq. 4).

$$P_N = e^{-\frac{(t-a)^2}{b^2}} \quad (\text{eq. 4})$$

The rate constant of the nucleation k_n is the reciprocal value of a ($k_n = 1/a$). The second term of eq. 3 describes the crystallization (k_g = growth rate constant, n = integer number (1, 2, 3) representing the growth dimension). We set n to 3 for consistency with the observed growth of cuboidal Co_3O_4 nanocrystals (see Figure S6). The resulting fits and the corresponding calculated probability of nucleation P_N are shown in Figures 4a and 4b, the latter becoming sharper with increasing temperature. For all temperatures, k_n remains smaller than k_g , i.e. nucleation is the rate-limiting step throughout. In line with the *Sharp-Hancock* plot trends, the rate constants derived from the *Gualtieri* model do not show a linear behavior in the Arrhenius plot either (Table 1 and Figure S2), and the values for k_n and k_g decrease at 200 °C.

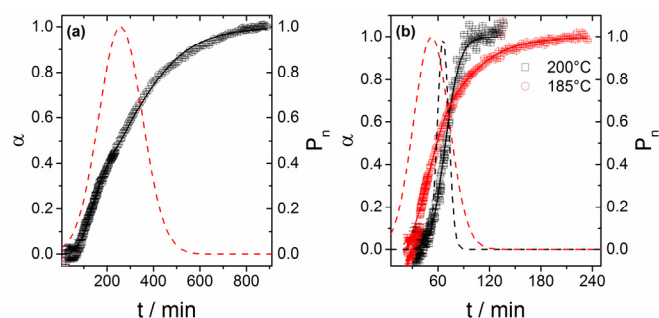


Figure 4. (a) Extent of reaction at 170°C vs. reaction time (black squares) fitted with the *Gualtieri* model (eq. 3), (b) extent of reaction at 185°C (red circles) and 200°C (black squares); solid line: fit, dashed line: nucleation probability P_N .

Table 1. Kinetic parameters obtained from *Sharp-Hancock* plots and from fits with the *Gualtieri* model.

	$T / ^\circ\text{C}$	170	185	200
	$t_0 / \text{min}^{[a]}$	58.5	29.2	39.8
	$t_{1/2} / \text{min}^{[a]}$	192.8	27.2	28.8
	growth model ^[b]	R ₃	F ₁	A ₂
<i>Sharp-Hancock</i>	$\ln(k)$	-5.57 ± 0.05	-3.71 ± 0.04	-3.5 ± 0.2
	n	1.20 ± 0.01	1.07 ± 0.01	2.37 ± 0.07
<i>Gualtieri</i> model	a / min	258 ± 1	52 ± 3	66 ± 6
	b / min	132 ± 2	29 ± 2	9.2 ± 0.2
	$k_g / 10^{-3} \text{ min}^{-1}$	8.0 ± 0.1	21.0 ± 0.7	18 ± 5
	$k_n / 10^{-3} \text{ min}^{-1}$	3.87 ± 0.02	19 ± 1	15 ± 1

[a] these values were determined by inspection of experimental data

[b] see Table S1

As this alternative data evaluation also substantiates a different growth mechanism taking over at 200 °C, isolated samples of

FULL PAPER

Co₃O₄ obtained in situ at different temperatures were subjected to ex situ analytical investigations in order to evaluate the impact of the mechanistic change on the materials properties.

The ex situ XRD patterns of these post-synthetic samples further prove their phase purity (see Figure S4), and their Raman spectra exhibit the characteristic transitions of Co₃O₄ (see Figure S5 and Table S3).^[40] Particle size distribution analysis of the TEM images of the cuboidal Co₃O₄ nanoparticles emerging from the in situ experiments (see Figure S6) resulted in mean particle sizes of 20.4 ± 3.7 nm and 19.5 ± 3.7 nm for the reactions at 170 °C and 185 °C, respectively (see Figure S7).^[41] Co₃O₄ nanoparticles formed at 200 °C exhibit a slightly higher mean particle size of 27.8 ± 5.7 nm. These TEM results are in line with the Scherrer-equation analysis of ex situ XRD data affording crystallite domain sizes of 14.3 ± 0.9 nm and 14.6 ± 1.0 nm for Co₃O₄ nanocrystals obtained at 170 °C and 185 °C, respectively, and a slightly higher crystallite size of 17.6 ± 1.5 nm at 200 °C (see Table S2).

BET measurements (Figure 3, inset) show a more significant difference between the samples emerging from both growth mechanism types (see Figure 3, inset). While the samples obtained at 170 °C and 185 °C show similar surface areas of 64 m²/g and 63 m²/g, respectively, Co₃O₄ obtained at 200 °C displays a significantly lower surface area of 38 m²/g. All in all, ex situ analyses (XRD, TEM and BET) show a correlation of Co₃O₄ nanoparticle properties and their underlying formation mechanisms, inducing a change towards slightly larger particles with significantly lower surface areas within the rather narrow preparative temperature window between 185 °C and 200 °C.

Quenching experiments on hydrothermal Co₃O₄ formation.

The most widespread approach towards optimization of hydrothermally synthesized materials is to change the synthesis parameters and to investigate the products post synthesis.^[21,23,42,43] Beyond this empirical approach, the above results illustrate that time-resolved PXRD measurements are a powerful tool to unravel growth mechanisms of such “black box” type synthetic methods.^[26,27] When applying these insights on conventional, non-monitored hydrothermal lab setups, their frequent sensitivity towards experimental parameter adjustments and scale-up should be taken into account.^[44] However, it is safe to assume that (a) the high-energy X-rays used in the above time-resolved PXRD measurements (65.6 keV) do not affect the time-scale of the crystallization and that (b) heating effects are negligible for the large solvent amounts used in the present study. Transferability of results from in situ energy dispersive XRD to home laboratory setups has been demonstrated in an earlier study by one of the authors on the hydrothermal crystallization of zeolite A.^[45] Likewise, kinetic information on MOF crystallization obtained with the same setup as in the present study were confirmed with lab-scale quenching experiments.^[31] Therefore, analogous hydrothermal quenching experiments were performed for temperatures and reagent volumes as applied during in situ monitoring, and the emerging cobalt oxide products were characterized ex situ with a wide range of analytical methods. The reaction times mentioned in the following correspond to the time after the autoclave reached the given holding temperature (170 °C, 185 °C, 200 °C).

Ex situ powder X-ray diffraction. Figure 5 compares the PXRD patterns of samples quenched from 170 °C and 185 °C after increasing reaction time to those of the corresponding in situ samples vs a reference Co₃O₄ pattern. Co₃O₄ adopts the normal spinel type structure, where the O²⁻ anions form a cubic closed-packed lattice with Co³⁺ cations occupying the octahedral sites and Co²⁺ cations located on the tetrahedral sites.^[42] Concerning hydrothermal Co₃O₄ synthesis at 170 °C and 185 °C, the first characteristic cobalt oxide spinel reflections appear after 20 min and 10 min of reaction time, respectively. When a reaction temperature of 200 °C is applied (see Figure S9), these reflections already occur at an effective reaction time of ca. 0 min (i.e. after immediate quenching when the holding temperature was reached), so that cobalt oxide spinel is already formed during the heating period. After 120 min of reaction time, characteristic peaks of Co(OH)₂ peaks are present, indicating the formation of impurities at 185 °C and 200 °C.

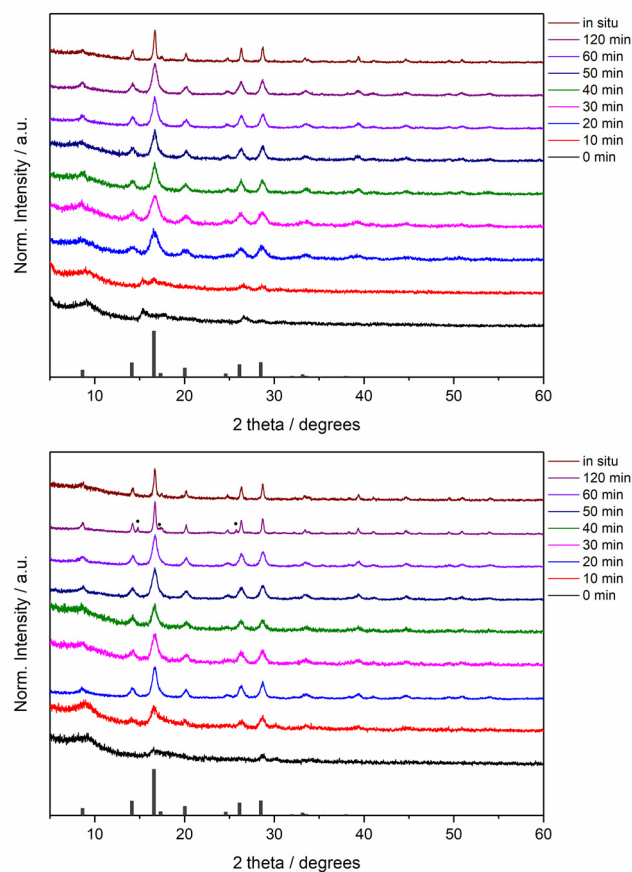


Figure 5. Ex situ PXRD patterns (MoK_{α1} radiation: $\lambda = 0.70926$ Å) of Co₃O₄ samples quenched from hydrothermal conditions after different reaction times (top: 170 °C, bottom: 185 °C; vertical bars: Bragg reflections of Co₃O₄ (PDF Card No.: 01-080-1544), * indicates Co(OH)₂ impurities (PDF-Card No.: 01-074-1057) in situ: samples recovered from the respective in situ experiments).

Likewise, additional CoO peaks appear for the reaction at 200 °C after 120 min (see Figure S10). This behavior stands in contrast to the in situ PXRD patterns (Figure 1), where spinel cobalt oxide is the only crystalline phase present at all temperatures, even

FULL PAPER

after notably longer reaction times (170 °C/900 min, 185 °C/240 min, 200 °C/170 min). A possible reason for these impurities could be the rapid cooling rate during the quenching. Visual comparison of the time-dependent ex situ PXRD patterns already clearly reveals that with prolonged reaction times, the peak shapes and their full width at half maximum (FWHM) become narrower. This corresponds to the evolution of the crystallite domain sizes D during the reaction that can be quantified using the Scherrer equation (see Table S2).^{[42],[46]} Concerning the evolution of the crystallite size over time (20 min, 40 min and 60 min), an increase at the onset of the 170 °C sample series from 3.9 ± 0.3 nm to 6.1 ± 0.1 nm was observed. Afterwards, the values remain within a range of ca. 6 nm, as observed for the entire series at 185 °C and 200 °C. Extended reaction times (120 min) lead to an increase in crystallite size up to 15.6 ± 0.8 nm and 17.3 ± 0.9 nm for 185 °C and 200 °C, respectively. These values are close to the final crystallite sizes of the Co_3O_4 samples formed in the in situ experiments.

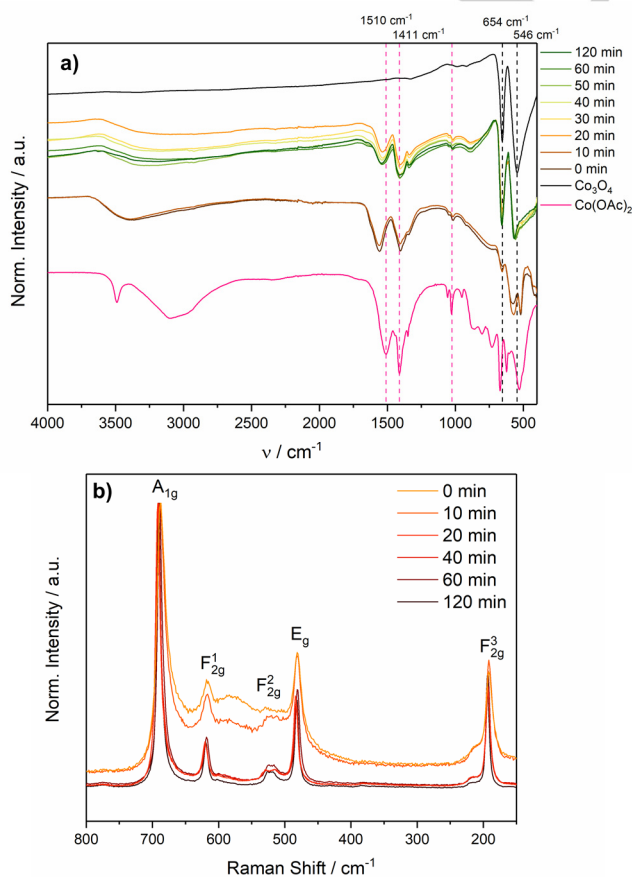


Figure 6. (a) FT-IR spectra and (b) Raman spectra (bottom) of Co_3O_4 samples synthesized under hydrothermal conditions for different reaction times at 170 °C compared to reference spectra of $\text{Co}(\text{OAc})_2$ and of commercial Co_3O_4 .

FT-IR and Raman analysis of quenched Co_3O_4 . Typical Co_3O_4 stretching vibration modes at 654 cm^{-1} $\nu(\text{Co}^{2+}_{\text{tetrahedral}}-\text{O})$ and 546 cm^{-1} $\nu(\text{Co}^{3+}_{\text{octahedral}}-\text{O})$ can be observed in Figure 6a after 20 min of reaction time, which corresponds with the timescale of Co_3O_4 formation evident from the ex situ PXRD pattern at 170 °C.^[47]

For the series of samples synthesized at 185 °C and 200 °C (see Figure S11), these distinctive signals can already be assigned after effective 0 min of reaction time (i.e. immediate quenching), which is in good accordance with the ex situ PXRD patterns of the 200 °C sample series.

Interestingly, the FT-IR spectra series of samples synthesized at 185 °C show the characteristic oxide peaks approx. 10 min earlier compared to the onset of according reflections in the PXRD pattern. A possible interpretation for this delay is the formation of an amorphous phase that cannot be detected in the PXRD pattern, or crystallites that are too small to be detected by Bragg diffraction, while already giving rise to Co_3O_4 signals in the FT-IR spectrum. The peaks at 1541 cm^{-1} , 1405 cm^{-1} , 1098 cm^{-1} , and 1040 cm^{-1} , correspond to stretching vibrations of carboxylate groups $\nu_a(\text{COO}^-)$ and $\nu_s(\text{COO}^-)$, as well as to a coupled stretch vibration $\nu(\text{C-C/O})$, respectively, which can be assigned to remnant acetate ions of the $\text{Co}(\text{OAc})_2$ precursor.^[6] Regardless of the reaction time and the reaction temperature, these carboxylate peaks persist in the FT-IR spectra, and they could not be removed through additional washing of the samples with either water, ethanol, or acetone. As no absorption of the carbonyl double bond around 1702 cm^{-1} was observed, the presence of neutral $-\text{COOH}$ can be excluded.

These results raise the questions of how acetate ions participate in the growth process of spinel cobalt oxide, and whether they represent an essential part of the functional catalyst structure. In a previous study, Co_3O_4 was synthesized under “one-pot” conditions in the presence of the surfactant polyoxyethylene (20) sorbitan trioleate (Tween-85). The authors reported on an organic coating of absorbed alkylated oleic carboxylate anions on the Co_3O_4 nanocubes arising from hydrolysis of Tween-85.^[48] Cobalt cations were proposed to serve as Lewis-acidic sites for the absorption of carboxylate and the formation of a surface complex. In this way, the acetate ions could act as capping molecules and thereby influence the shape of the nanoparticles.^[49] In a more recent study Viljoen et al. demonstrated that the cubic shape of the nanoparticles is directly influenced by the acetate precursor type used during the synthesis.^[50]

Raman spectra of the sample series quenched from 170 °C are shown in Figure 6b and those of the sample series quenched at 185 °C and 200 °C are summarized in Figure S12. Interestingly, all three sample series show the same trend over the entire temperature range, i.e. already after virtually 0 min of effective reaction time after heating, peaks occur which agree well with the predicted phonon modes $A_{1g} + F_{2g}^1 + F_{2g}^2 + E_g + F_{3g}^3$ of spinel type Co_3O_4 ,^[40,43] as well as with other reports for Raman spectra of Co_3O_4 nanoparticles.^[51] The band at 690 cm^{-1} can be assigned to the symmetric $\text{Co}^{3+}-\text{O}$ stretching vibration of the octahedral sites of the A_{1g} species in O_h spectroscopic symmetry.^[52] The medium intensity bands at 481 cm^{-1} , 619 cm^{-1} and the weak intensity band at 520 cm^{-1} display E_g , F_{2g}^1 , and F_{2g}^2 symmetry, respectively. The band at 193 cm^{-1} is typical for the tetrahedral sites (CoO_4) with F_{2g}^3 symmetry. The same tendency can be observed in Table S3 where the FWHM of the given Raman modes (A_{1g} , F_{2g}^1 , E_g , F_{3g}^3) decreases with increasing reaction time (with a few deviations for 40 min and 60 min at 185 °C and 200 °C, respectively). This decrease indicates a reduction of internal defects in the Co_3O_4

FULL PAPER

nanoparticles, resulting in a higher crystallinity, which agrees well with the ex situ PXRD measurements (Figures 7 and S9).^[53] In contrast to the above discussed FT-IR spectra, acetate signals could not be observed in the Raman spectra.^[54] This is probably due to the very low intensity vibrations of the small acetate amounts compared to the overwhelming Raman intensity of the main phase Co_3O_4 .^[55]

Elemental and TGA analysis of the quenched Co_3O_4 particles.

To obtain more information on the role of acetate precursor ions in spinel cobalt oxide formation, elemental analysis (EA) as well as thermogravimetric analysis/differential scanning calorimetry (TGA/DSC) were performed on selected samples covering all synthesis temperatures, and the results are summarized together with elemental analysis results in Table 2. First, significant amounts of carbon and hydrogen were present at a reaction time of approx. 0 min after heating to all three temperatures, together with negligible nitrogen amount for all measurements. Upon longer reaction times (60 min), the Co_3O_4 samples contain less carbon and hydrogen, indicating a decrease of acetate content. TGA measurements confirm the above trend through a considerable decrease in mass loss at longer reaction times for all synthesis temperatures, and Figure 7 compares the obtained DSC, DTG, and TGA curves up to the end of the exothermic acetate decomposition.^[56]

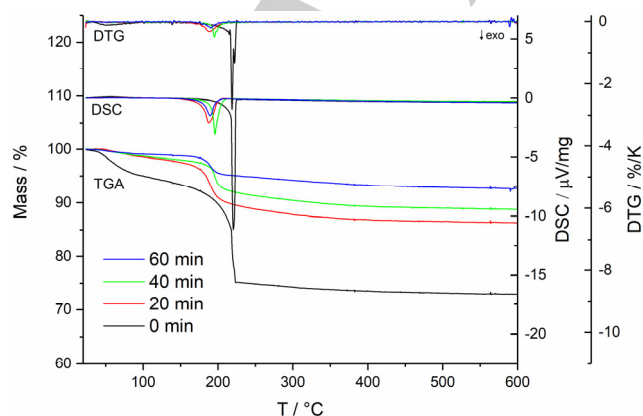


Figure 7. Thermoanalysis of Co_3O_4 synthesized under hydrothermal conditions over different reaction times at 170 °C.

All samples show a small mass loss at around 90 °C, which can be assigned to dehydration, followed by a substantial mass loss accompanied by a strong exothermic peak arising from the combustion of organic matter (acetate).^[57] Analogous trends are present in the 185 °C and 200 °C sample series (see Figure S13). Elemental analysis after the TGA measurements showed negligible C/H/N amounts, thus confirming total combustion of organic matter in the sample.

Table 2. Results of thermogravimetric analysis (TGA mass loss) and elemental analysis for Co_3O_4 samples after different reaction times.

T / °C	t / min	C / wt%	H / wt%	N / wt%	TGA ^[a] / %
170	0	7.95	1.73	0.11	18.6
	60	2.65	0.70	0.23	3.9
185	0	7.74	2.36	0.20	21.0
	60	2.77	0.75	0.03	5.4
200	0	8.14	2.53	0.14	22.1
	60	1.97	0.55	0.1	2.9

[a] Mass loss over a temperature range from 140 – 240 °C.

XPS analysis of Co_3O_4 nanoparticles. The persistence of the acetate signals after washing steps with different solvents called for XPS measurements to check for the presence of acetate ions on the surface of the Co_3O_4 nanocubes as possible chemisorbed “capping” agents.^[48]

The O 1s spectra in Figure 8a-c show two overlapping peaks at 529 eV and 531 eV. The peak at 529 eV can be typically assigned to lattice oxygen of Co_3O_4 , whereas the peak at 531 eV can contain signals of absorbed surface oxygen as well as of acetate oxygen.^[48,58] The C 1s spectra in Figure 8d-f show two peaks at 285 eV and 288 eV, which can be assigned to the $-\text{COO}^-$ and $-\text{CH}_3$ or $-\text{C}-\text{C}-$ moieties of acetate, respectively.^[59] These results further demonstrate that the presence of acetate ions as chemisorbed “capping” agents on the surface of the Co_3O_4 nanocubes is a possibility.

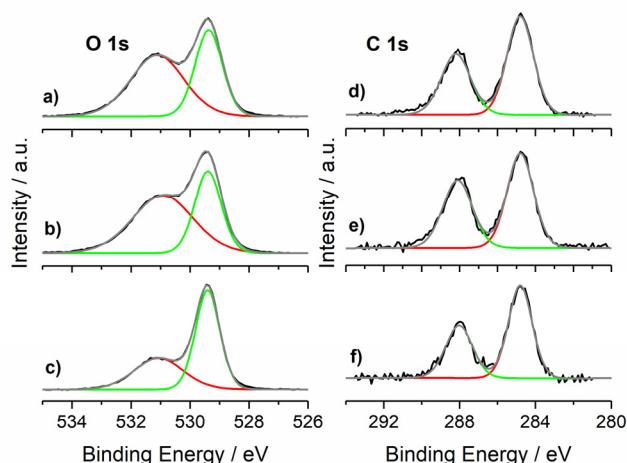


Figure 8. XPS investigation of O 1s and C 1s peaks for quenched Co_3O_4 samples synthesized at 170 °C for (a)/(d) 20 min, (b)/(e) 60 min, and for (c)/(f) Co_3O_4 samples obtained after the in situ experiment at 170 °C.

Morphology of as-synthesized Co_3O_4 nanoparticles. TEM images of Co_3O_4 samples after 0 min and 60 min reaction reveal the presence of agglomerated nanoparticles for all three reaction temperatures (Figure 9a-f). Compared to samples obtained after

FULL PAPER

ca. 0 min reaction time, the particles formed after 60 min are more crystalline, larger and cuboidal, as observed during the in situ studies (Figure S6) and in previous reports.^[21,23] The crystalline character of the sample prepared at 170 °C and 60 min reaction time is verified by the HRTEM images in Figure 9g. In the expanded region of the image (Figure 9h), the nanocube is shown to exhibit a lattice spacing of 0.29 nm that corresponds to the (220) planes of spinel-type Co_3O_4 . The calculated values for the crystallite sizes (Tables S2 and S4) are in good agreement with particle size distributions determined from TEM images (Figure S8).

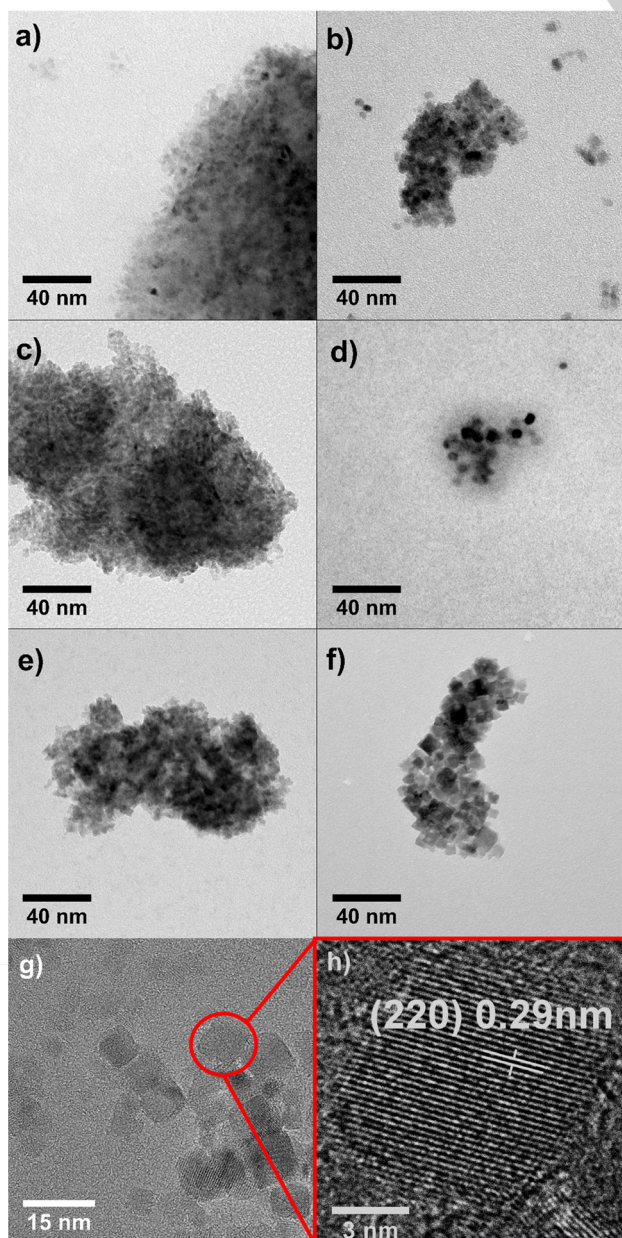


Figure 9. Selection of TEM images of Co_3O_4 synthesized under hydrothermal conditions. 170 °C: (a) 0 min, (b) 60 min; 185 °C: (c) 0 min, (d) 60 min; 200 °C: (e) 0 min, (f) 60 min; and HRTEM image at 170 °C: (g) 60 min, (h) inset: area with lattice spacing of 0.29 nm.

Likewise, BET surface areas (Tables S2 and S4) show an effective trend towards lower values with longer reaction time at the given temperatures (with only slight deviations within the individual series).

Photocatalytic water oxidation activity. As mentioned above, the water oxidation activity of spinel-type oxide catalysts depends on a wide range of parameters, including morphology, surface area/particle size, valence states, crystallinity, defects/interstitials and site occupancies/inversion. Given that the mechanisms of most heterogeneous water oxidation catalysts are not yet fully understood, empirical control over structure-activity relationships through optimized synthetic parameters is highly sought-after.

The water oxidation performance of Co_3O_4 nanoparticles obtained in this study is correlated with key materials parameters and synthetic conditions in Figure 10 and Table S4.

Concerning the O_2 yield as a function of quenching reaction temperature/time, prolonged treatment at 170 °C leads to steadily increasing yields, while Co_3O_4 catalysts synthesized at 185 °C and 200 °C peak after 20 min of reaction time, respectively. Most importantly, samples treated for significant times conventionally at 200 °C always afford lower O_2 yields than those obtained at 170 °C or 185 °C. This corresponds well with the notably lower O_2 yields of Co_3O_4 nanoparticles collected from in situ experiments at 200 °C compared to those grown at 170 °C or 185 °C (Figure 10 and Table S4).

Regarding the correlation between BET surface area and O_2 yields of catalysts from conventional hydrothermal conditions, the respective maximum yields after 20 min of treatment do not go hand in hand with the respective maximum BET surface area values within the series. For cobalt oxide samples synthesized at 170 °C, the yields are even slightly increasing with lower BET values. In short, there is no clear trend among all three ex situ synthesis temperatures and the resulting BET surfaces do not appear to exert a systematic influence on the performance. In contrast, the drastic activity loss for Co_3O_4 nanoparticles obtained under in situ conditions at 200 °C goes hand in hand with a significantly lower BET surface area (Figure 10 and Table S4).

The crystallite size does not undergo a significant change for the sample series at 185 °C and 200 °C, and the sharp increase of crystallite size for treatments longer than 20 min at 170 °C does not exert a comparable effect on the performance trend. Related observations were made for the Co_3O_4 materials isolated from in situ conditions.

With respect to the absolute O_2 yield values, it is striking that the cobalt oxide sample quenched at 170 °C after virtually 0 min of reaction time after heating already affords a yield that is close to the maximum yield within the 200 °C series. Two conclusions can be drawn from the above trends. First, the reaction temperature seems to be the most influential performance parameter, followed by the treatment time. Second, the high initial activity of low crystalline cobalt phases obtained at 170 °C (Figure 5, top) suggests that such quasi amorphous phases may be superior to crystalline cobalt oxides, in line with recent discussions in the field.^[60]

When comparing the absolute yields of the Co_3O_4 water oxidation catalysts summarized here to related systems using the

FULL PAPER

[Ru(bpy)₃]²⁺/S₂O₈²⁻ performance assay, they are in a league with other highly active earth-abundant transition metal oxide WOCs and with heterogeneous catalysts derived from molecular precatalysts and homogeneous catalysts.^[2]

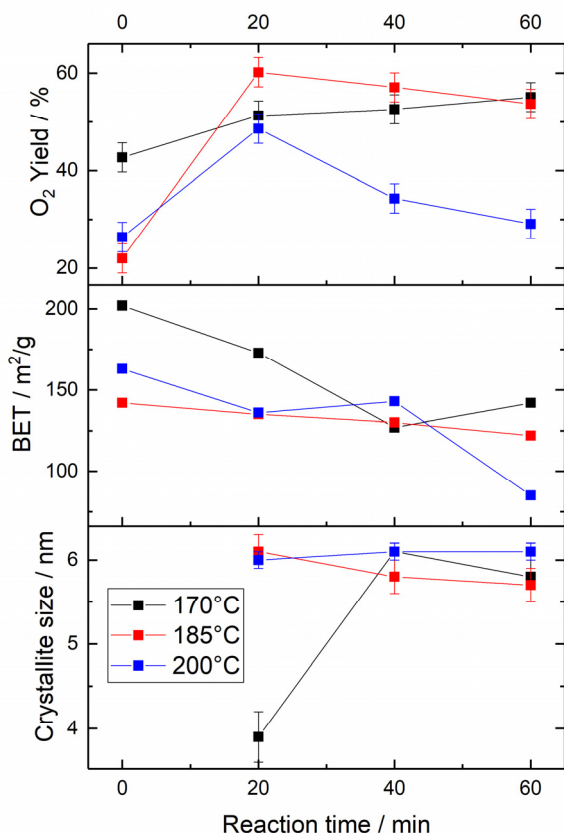


Figure 10. Photocatalytic activity, BET surface, and crystallite size as a function of reaction time.

As the influence of the amorphous acetate-containing phases on the photocatalytic activity cannot be assessed with the help of in situ PXRD data, additional hydrothermal syntheses were performed to synthesize cobalt oxide under similar conditions using Co(NO₃)₂ as a precursor. The samples synthesized at 180 °C and 10 min, 30 min, and 60 min reaction time were characterized by PXRD (Figure S15), FT-IR (Figure S16), and Raman analysis (Figure S17). At 10 min reaction time the sample is amorphous, while pure Co₃O₄ is present after 30 min and 60 min. The decreasing BET surface area over time is not directly correlated with the activity trend (Table S4). The amorphous sample (obtained after 10 min) affords a rather high O₂ yield of 53.3 %. This indicates that acetate as a counteranion does not exert a significant influence on the oxygen evolution activity of the mainly amorphous cobalt oxide samples.

Conclusions

The present study on the hydrothermal growth processes of nanoscale Co₃O₄ water oxidation catalysts from cobalt acetate precursors aimed to transfer new insights from time-resolved PXRD monitoring on optimized lab-scale catalyst production. The key information derived from time-resolved PXRD data is a change in the hydrothermal Co₃O₄ growth mechanism between 185 °C and 200 °C that clearly emerges from the analysis of the (311) reflection with two different models (*Sharp-Hancock* and *Gualtieri*). Follow-up analyses showed that the mechanistic change from a first-order model F₁ at ≤ 185 °C to JMAK growth kinetics A₂ at 200 °C goes hand in hand with a drastic decrease in surface area and a sharp drop in the photocatalytic performance of the Co₃O₄ nanomaterials. Complementary quenching studies demonstrated that the synthetic temperature threshold of 200 °C determined from in situ experiments also serves as a guideline for conventional Co₃O₄ WOC synthesis in the present cobalt acetate hydrothermal system. The photocatalytic activity trends after 60 min of conventional treatment correspond well with those of Co₃O₄ WOCs generated during the in situ experiment, while prolonged reaction times are less favorable. Furthermore, the investigation of quenched cobalt oxide samples with a wide range of analytical methods indicates that amorphous cobalt oxide materials formed in the very early stages of the reaction already display oxygen yields in the range of crystalline Co₃O₄ samples produced within the stable 170 – 185 °C temperature window. However, a significant influence of acetate counteranions on the photocatalytic Co₃O₄ performance could be excluded through reference experiments.

Overall, we demonstrate that complex and parameter-sensitive hydrothermal WOC formation processes can be controlled through efficient combination of mechanistic in situ studies with comprehensive ex situ analyses. The emerging precise information about optimal hydrothermal temperature windows for enhanced WOC performance is essential for efficient larger scale catalyst production. Further investigations are now in progress to clarify the optimal ratio of crystalline and amorphous cobalt oxide catalysts in the present cobalt acetate hydrothermal system for application-oriented recycling and scalability studies.

Experimental Section

Materials and instruments: All chemicals and solvents were purchased from commercial suppliers: [Ru(bpy)₃]Cl₂·6H₂O (Sigma-Aldrich, 99.95%), Na₂S₂O₈ (Sigma-Aldrich, ≥99.0%), Co(OAc)₂·4H₂O (Sigma-Aldrich, ≥98.0%), Co₃O₄ (Alfa Aesar, 99%), Co(NO₃)₂·6H₂O (Sigma-Aldrich, ≥99.0%), H₂O₂ 30 wt.% in H₂O (Sigma-Aldrich, ACS reagent), ammonia solution 25% (Merck, for analysis), ethanol (VWR Chemicals, absolute). Raman spectra were recorded using a Renishaw inVia Qontor confocal Raman microscope equipped with a diode laser (785 nm). Nitrogen sorption isotherms were recorded after degassing at 100 °C for 20 h under vacuum by using a Quantachrome Quadrasorb SI porosimeter at 77 K. Adsorption branch points (0.05 < p/p₀ < 0.3) were applied in the BET model to calculate the apparent surface area. Ex situ PXRD patterns were recorded using a STOE STADI P diffractometer in transmission mode (flat-plate sample holder, Ge monochromator, and MoK_{α1} radiation) using a position sensitive

FULL PAPER

microstrip solid-state detector (MYTHEN 1K). Attenuated total reflectance Fourier-transform infrared (ATR-FT-IR) spectra were recorded on a Bruker Vertex 70 spectrometer equipped with a Platinum ATR accessory containing a diamond crystal. Thermogravimetric (TG) analyses were performed on a Netzsch STA Jupiter 449 F3 TGA in the temperature range 298 to 873 K with a heating rate of 2 K min⁻¹ in air atmosphere in an Al₂O₃ crucible. GC measurements were recorded using an Agilent Technologies 7820A equipped with a thermal conductivity detector and a 30 m * 0.53 mm packed HP molecular sieve column with a 50.0 µm film and helium carrier gas (purity 6.0). Transmission electron microscopy (TEM) images were taken using a JEOL JEM-1400 Plus equipped with a LaB₆ crystal as emitter (120 kV) and a JEOL CCD camera Ruby (8 M pixel). Elemental analyses were performed on a LECO TruSpec Micro. X-ray photoelectron spectroscopy (XPS) was conducted on selected samples using a Physical Electronics Quantum 2000 X-ray photoelectron spectrometer featuring monochromatic Al K_α radiation, generated from an electron beam operated at 15 kV and 32.3 W. HRTEM investigations were performed with a FEI Talos F200X (200kV) high-resolution transmission electron microscope (HRTEM). Samples were deposited on a 400 mesh copper grid, which is covered by ultra-thin carbon support film (3 nm thickness).

Time-resolved X-ray diffraction: The time-resolved PXRD experiments were performed at the I12 beamline at the Diamond Light Source, UK.^[35] The solvothermal reaction was carried out using a stainless steel autoclave in the Oxford-Diamond in situ cell (ODISC).^[34] X-rays with an energy of 65.6 keV ($\lambda = 0.18893$ Å) were used in order to penetrate the stainless steel autoclave. Hydrothermal formation of Co₃O₄ was carried out according to a previous procedure.^[23] This reaction was studied at different temperatures from 170 °C to 200 °C. In a typical experiment Co(OAc)₂·4H₂O (747 mg, 3 mmol) was dissolved in solvent mixture (1.63 mL H₂O, 0.37 mL NH₃ 35% and 0.5 mL H₂O₂ (30 %)). After 2 h of stirring in the PTFE liner at room temperature, 7.5 mL ethanol were added and the reaction mixture was placed in the stainless steel autoclave. The reaction mixture was rapidly heated up to the desired temperatures, controlled via a PID controller and a thermocouple mounted close to the cell wall using the infrared lamps of the ODISC cell. The diffraction patterns were recorded in 12.44 s acquisitions using a fast two-dimensional detector (Thales Pixium RF4343) which had been calibrated using a NIST CeO₂ reference. Data were normalised and analyzed using the DAWN software.^[61]

Quenching experiments: The quenching experiments were carried out according to a previous procedure.^[23] Co(OAc)₂·4H₂O (747 mg, 3 mmol) was dissolved in deionized H₂O (1.5 mL), afterwards NH₃ (0.5 mL, 25 wt%) and H₂O₂ (0.5 mL, 30 %) were added and the solution was stirred for 2 h. Finally, ethanol (absolute, 7.5 mL) was added and the reaction mixture was transferred to a 15 mL PTFE-lined stainless steel autoclave. The autoclave was heated to and maintained at the given temperature (170 °C, 185 °C, 200 °C) in an oven (Binder) for the given time (start temp. 23 °C, heating rate 5 K min⁻¹). After reaching the holding temperature (170 °C, 185 °C, 200 °C; start reaction time) the autoclaves were removed from the oven in time intervals of 10 min between 0 min reaction time and 60 min reaction time as well as 120 min reaction time. The reaction was quenched by cooling down the autoclave rapidly under cold running water (10 °C) for 10 min. The resulting product was isolated by centrifugation (5000 rpm for 12 min), washed three times (once with deionized H₂O, twice with acetone) and dried at 78 °C for 16 h in air.

Quenching experiments with Co(NO₃)₂ as precursor: For the synthesis of Co₃O₄ with a different precursor, Co(NO₃)₂·6H₂O (244 mg, 0.84 mmol) was dissolved in deionized H₂O (7.0 mL), and afterwards NH₃ (1.6 mL, 25 wt%) and H₂O₂ (0.5 mL, 30 %) were added to the solution, respectively. Finally, more NH₃ (1.4 mL, 25 wt%) was added until pH 11 was reached.

The reaction mixture was transferred to a 15 mL PTFE-lined stainless steel autoclave. From this point onward the experiments were handled like previously described in the quenching experiments part, except that the reaction temperature was 180 °C for reaction times of 10 min, 30 min, and 60 min.

Photocatalytic tests: For evaluating the water oxidation activity of the synthesized samples a standard [Ru(bpy)₃]²⁺/S₂O₈²⁻ protocol was used.^[62] Photocatalytic reaction suspensions were prepared under exclusion of light in a dark environment. Following the protocol, oxide photocatalyst (2.00 mg, 8.3 µmol), [Ru(bpy)₃]Cl₂·6H₂O photosensitizer (6.0 mg, 1 mM) and Na₂S₂O₈ sacrificial electron acceptor (9.5 mg, 5 mM) were mixed with borate buffer (8 mL, 85 mM, pH 8.5) in a 10 mL glass vial. Afterwards, glass vials containing the suspension were sealed gastight with a rubber septum (PTFE) and an aluminum crimp cap, sonicated for 3 min and degassed through purging with helium (purity 5.0) for 10 min to remove oxygen from the solution and the head space of the vial. Catalytic reactions were initiated by illuminating the catalytic suspension with a 460 nm high flux LED light (26.1 mW/cm², Rhopoint Components LTD) under a constant stirring rate of 1200 rpm. After 25 min illumination time, a 100 µL gas sample of the headspace was taken with a gastight microliter syringe (Hamilton-1825RN) and injected into the gas chromatograph. To quantify the oxygen evolution a previously determined linear GC calibration curve was used and air contamination was corrected.

Acknowledgements

L.R., K.L., R.M., and G.R.P. thank the UZH research priority program *Solar Light to Chemical Energy Conversion* (URPP LightChEC) for financial support. G.R.P. is grateful to the Swiss National Science Foundation (Sinergia Grant No. CRSII2_160801/1) for financial support. We thank Diamond Light Source for permission of beamtime (EE12884). The authors thank Oxana V. Magdysyuk (Diamond) for support during beamtime. All microscopy work was carried out at the Scientific Center for Optical and Electron Microscopy (ScopeM) at ETH Zurich. Additionally, the authors thank S. Esmael Balaghi for taking the HRTEM images, Sebastian Siol (EMPA) for conducting the XPS experiments, Jarpla Madhusudhan Naik for performing the thermoanalysis measurements, and Catherine Witteveen for performing reference hydrothermal experiments. Elemental analyses were performed by the Molecular and Biomolecular Analysis Service (MoBiAS) at ETH Zurich.

Keywords: In situ monitoring • hydrothermal • nanoparticle formation mechanisms • photocatalysis • cobalt oxide • water oxidation

- [1] a) J. Li, R. Güttinger, R. Moré, F. Song, W. Wan, G. R. Patzke, *Chem. Soc. Rev.* **2017**; b) G. W. Brudvig, S. Campagna, *Chem. Soc. Rev.* **2017**, 46(20), 6085–6087; c) K. Kalyanasundaram, M. Graetzel, *Curr. Opin. Biotechnol.* **2010**, 21(3), 298–310; d) Y. Tachibana, L. Vayssieres, J. R. Durrant, *Nat. Photonics* **2012**, 6(8), 511–518; e) A. Kudo, Y. Miseki, *Chem. Soc. Rev.* **2009**, 38(1), 253–278;
- [2] S. Fukuzumi, J. Jung, Y. Yamada, T. Kojima, W. Nam, *Chem. - Asian J.* **2016**, 11(8), 1138–1150.

FULL PAPER

- [3] a) P. Garrido-Barros, C. Gimbert-Suriñach, R. Matheu, X. Sala, A. Llobet, *Chem. Soc. Rev.* **2017**, 46(20), 6088–6098; b) B. M. Hunter, H. B. Gray, A. M. Müller, *Chem. Rev.* **2016**, 116(22), 14120–14136; c) N.-T. Suen, S.-F. Hung, Q. Quan, N. Zhang, Y.-J. Xu, H. M. Chen, *Chem. Soc. Rev.* **2017**, 46(2), 337–365; d) K. L. Materna, R. H. Crabtree, G. W. Brudvig, *Chem. Soc. Rev.* **2017**, 46(20), 6099–6110;
- [4] a) P. Du, R. Eisenberg, *Energy Environ. Sci.* **2012**, 5(3), 6012; b) A. Singh, L. Spiccia, *Coord. Chem. Rev.* **2013**, 257(17–18), 2607–2622; c) X. Deng, H. Tüysüz, *ACS Catal.* **2014**, 4(10), 3701–3714; d) J. R. Galán-Mascarós, *ChemElectroChem* **2015**, 2(1), 37–50; e) M. Grzelczak, J. Zhang, J. Pfrommer, J. Hartmann, M. Driess, M. Antonietti, X. Wang, *ACS Catal.* **2013**, 3(3), 383–388; f) M. Zhang, M. de Respinis, H. Frei, *Nature Chem.* **2014**, 6(4), 362–367;
- [5] a) W. Y. Li, L. N. Xu, J. Chen, *Adv. Funct. Mater.* **2005**, 15(5), 851–857; b) Y. Liu, G. Zhu, B. Ge, H. Zhou, A. Yuan, X. Shen, *CrystEngComm* **2012**, 14(19), 6264;
- [6] A.-M. Cao, J.-S. Hu, H.-P. Liang, W.-G. Song, L.-J. Wan, X.-L. He, X.-G. Gao, S.-H. Xia, *J. Phys. Chem. B* **2006**, 110(32), 15858–15863.
- [7] a) X. W. Lou, D. Deng, J. Y. Lee, J. Feng, L. A. Archer, *Adv. Mater.* **2008**, 20(2), 258–262; b) D. Su, X. Xie, P. Munroe, S. Dou, G. Wang, *Sci. Rep.* **2014**, 4, 6519;
- [8] R. M. Wang, C. M. Liu, H. Z. Zhang, C. P. Chen, L. Guo, H. B. Xu, S. H. Yang, *Appl. Phys. Lett.* **2004**, 85(11), 2080.
- [9] a) V. R. Mate, M. Shirai, C. V. Rode, *Catal. Commun.* **2013**, 33, 66–69; b) X. Xie, Y. Li, Z.-Q. Liu, M. Haruta, W. Shen, *Nature* **2009**, 458(7239), 746–749;
- [10] L. Hu, K. Sun, Q. Peng, B. Xu, Y. Li, *Nano Res.* **2010**, 3(5), 363–368.
- [11] H. Zhao, Y.-P. Zhu, Z.-Y. Yuan, *Eur. J. Inorg. Chem.* **2016**, 2016(13–14), 1916–1923.
- [12] a) S. S. K. Ma, T. Hisatomi, K. Maeda, Y. Moriya, K. Domen, *J. Am. Chem. Soc.* **2012**, 134(49), 19993–19996; b) C. S. Chua, D. Ansovini, C. J. J. Lee, Y. T. Teng, L. T. Ong, D. Chi, T. S. A. Hor, R. Raja, Y.-F. Lim, *Phys. Chem. Chem. Phys.* **2016**, 18(7), 5172–5178;
- [13] P. W. Menezes, A. Indra, A. Bergmann, P. Chernev, C. Walter, H. Dau, P. Strasser, M. Driess, *J. Mater. Chem. A* **2016**, 4(25), 10014–10022.
- [14] a) D. M. Robinson, Y. B. Go, M. Mui, G. Gardner, Z. Zhang, D. Mastrogianni, E. Garfunkel, J. Li, M. Greenblatt, G. C. Dismukes, *J. Am. Chem. Soc.* **2013**, 135(9), 3494–3501; b) C. P. Plaisance, R. A. van Santen, *J. Am. Chem. Soc.* **2015**, 137(46), 14660–14672;
- [15] a) P. Du, O. Kokhan, K. W. Chapman, P. J. Chupas, D. M. Tiede, *J. Am. Chem. Soc.* **2012**, 134(27), 11096–11099; b) G. George, S. Anandhan, *J. Sol-Gel Sci. Technol.* **2013**, 67(2), 256–266;
- [16] a) Y.-F. Li, Z.-P. Liu, *J. Am. Chem. Soc.* **2011**, 133(39), 15743–15752; b) S. Farhadi, K. Pourzare, S. Bazgir, *J. Alloys Compd.* **2014**, 587, 632–637; c) A. S. Schenk, S. Eiben, M. Goll, L. Reith, A. N. Kulak, F. C. Meldrum, H. Jeske, C. Wege, S. Ludwigs, *Nanoscale* **2017**, 9(19), 6334–6345; d) E. Edri, J. K. Cooper, I. D. Sharp, D. M. Guldli, H. Frei, *J. Am. Chem. Soc.* **2017**, 139(15), 5458–5466; e) H. H. Pham, M.-J. Cheng, H. Frei, L.-W. Wang, *ACS Catal.* **2016**, 6(8), 5610–5617;
- [17] X. Xiao, X. Liu, H. Zhao, D. Chen, F. Liu, J. Xiang, Z. Hu, Y. Li, *Adv. Mater.* **2012**, 24(42), 5762–5766.
- [18] a) L. Xu, Q. Jiang, Z. Xiao, X. Li, J. Huo, S. Wang, L. Dai, *Angew. Chem.* **2016**, 128(17), 5363–5367; b) X. Deng, R. Rin, J.-C. Tseng, C. Weidenthaler, U.-P. Apfel, H. Tüysüz, *ChemCatChem* **2017**, 9(22), 4238–4243; c) F. Jiao, H. Frei, *Angew. Chem. Int. Ed.* **2009**, 48(10), 1841–1844;
- [19] a) N. Bahlawane, E. Fischer Rivera, K. Kohse-Höinghaus, A. Brechling, U. Kleineberg, *Appl. Cat. B* **2004**, 53(4), 245–255; b) G. Binotto, D. Larcher, A. S. Prakash, R. Herrera Urbina, M. S. Hegde, J.-M. Tarascon, *Chem. Mater.* **2007**, 19(12), 3032–3040; c) K. Ding, X. Zhang, P. Yang, X. Cheng, *CrystEngComm* **2016**, 18(42), 8253–8261; d) T. Ghosh, S. K. Dash, P. Chakraborty, A. Guha, K. Kawaguchi, S. Roy, T. Chattopadhyay, D. Das, *RSC Adv.* **2014**, 4(29), 15022–15029; e) C. Guan, X. Qian, X. Wang, Y. Cao, Q. Zhang, A. Li, J. Wang, *Nanotechnol.* **2015**, 26(9), 94001; f) M. Hamdani, R. N. Singh, P. Chartier, *Int. J. Electrochem. Sci.* **2010**, 5, 556–577; g) B. Han, J.-M. Park, K. H. Choi, W.-K. Lim, T. R. Mayangsari, W. Koh, W.-J. Lee, *Thin Solid Films* **2015**, 589, 718–722; h) J. A. Koza, Z. He, A. S. Miller, J. A. Switzer, *Chem. Mater.* **2012**, 24(18), 3567–3573; i) A. U. Mane, K. Shalini, A. Wohlfart, A. Devi, S. A. Shivashankar, *J. Cryst. Growth* **2002**, 240(1–2), 157–163; j) V. R. Shinde, S. B. Mahadik, T. P. Gujar, C. D. Lokhande, *Appl. Surf. Sci.* **2006**, 252(20), 7487–7492; k) D. Wang, Q. Wang, T. Wang, *Inorg. Chem.* **2011**, 50(14), 6482–6492; l) J. B. Wu, Y. Lin, X. H. Xia, J. Y. Xu, Q. Y. Shi, *Electrochim. Acta* **2011**, 56(20), 7163–7170;
- [20] X. Wang, J. Zhuang, Q. Peng, Y. Li, *Nature* **2005**, 437(7055), 121–124.
- [21] Y. Dong, K. He, L. Yin, A. Zhang, *Nanotechnology* **2007**, 18(43), 435602.
- [22] a) L. Hu, Q. Peng, Y. Li, *J. Am. Chem. Soc.* **2008**, 130(48), 16136–16137; b) J. Jiang, J. P. Liu, X. T. Huang, Y. Y. Li, R. M. Ding, X. X. Ji, Y. Y. Hu, Q. B. Chi, Z. H. Zhu, *Cryst. Growth Des.* **2010**, 10(1), 70–75; c) X.-h. Xia, J.-p. Tu, Y.-j. Mai, X.-l. Wang, C.-d. Gu, X.-b. Zhao, *J. Mater. Chem.* **2011**, 21(25), 9319; d) G. Wang, X. Shen, J. Horvat, B. Wang, H. Liu, D. Wexler, J. Yao, *J. Phys. Chem. C* **2009**, 113(11), 4357–4361; e) Y. Teng, S. Yamamoto, Y. Kusano, M. Azuma, Y. Shimakawa, *Mater. Lett.* **2010**, 64(3), 239–242;
- [23] H. Liu, G. R. Patzke, *Chem. - Asian J.* **2014**, 9(8), 2249–2259.
- [24] K. M. Ø. Jensen, C. Tyrsted, M. Bremholm, B. B. Iversen, *ChemSusChem* **2014**, 7(6), 1594–1611.
- [25] D. S. Cook, Y. Wu, K. Lienau, R. Moré, R. J. Kashtiban, O. V. Magdysyuk, G. R. Patzke, R. I. Walton, *Chem. Mater.* **2017**, 29(12), 5053–5057.
- [26] Y. Zhou, E. Antonova, W. Bensch, G. R. Patzke, *Nanoscale* **2010**, 2(11), 2412–2417.
- [27] N. Pienack, W. Bensch, *Angew. Chem. Int. Ed.* **2011**, 50(9), 2014–2034.
- [28] A. F. Gualtieri, *Phys. Chem. Miner.* **2001**, 28(10), 719–728.
- [29] H. Reinsch, N. Stock, *CrystEngComm* **2013**, 15(3), 544–550.
- [30] G. Zahn, P. Zerner, J. Lippke, F. L. Kempf, S. Lilienthal, C. A. Schröder, A. M. Schneider, P. Behrens, *CrystEngComm* **2014**, 16(39), 9198–9207.
- [31] Y. Wu, M. I. Breeze, G. J. Clarkson, F. Millange, D. O'Hare, R. I. Walton, *Angew. Chem. Int. Ed.* **2016**, 55(16), 4992–4996.
- [32] M. Wendt, L. K. Mahnke, N. Heidenreich, W. Bensch, *Eur. J. Inorg. Chem.* **2016**, 2016(34), 5393–5398.
- [33] a) J. Rostgaard Eltzholtz, C. Tyrsted, K. M. Ørnsbjerg Jensen, M. Bremholm, M. Christensen, J. Becker-Christensen, B. Brummerstedt Iversen, *Nanoscale* **2013**, 5(6), 2372–2378; b) D. R. Hummer, P. J. Heaney, J. E. Post, *J. Cryst. Growth* **2012**, 344(1), 51–58; c) K. M. Ø. Jensen, M. Christensen, P. Juhas, C. Tyrsted, E. D. Bøjesen, N. Lock, S. J. L. Billinge, B. B. Iversen, *J. Am. Chem. Soc.* **2012**, 134(15), 6785–6792; d) J.-L. Mi, C. Clausen, M. Bremholm, N. Lock, K. M. Ø. Jensen, M. Christensen, B. B. Iversen, *Cryst. Growth Des.* **2012**, 12(12), 6092–6097; e) J.-L. Mi, M. Christensen, C. Tyrsted, K. Ø. Jensen, J. Becker, P. Hald, B. B. Iversen, *J. Phys. Chem. C* **2010**, 114(28), 12133–12138;
- [34] S. J. Moorhouse, N. Vranješ, A. Jupe, M. Drakopoulos, D. O'Hare, *Rev. Sci. Instr.* **2012**, 83(8), 84101.
- [35] M. Drakopoulos, T. Connolly, C. Reinhard, R. Atwood, O. Magdysyuk, N. Vo, M. Hart, L. Connor, B. Humphreys, G. Howell, S. Davies, T. Hill, G. Wilkin, U. Pedersen, A. Foster, N. de Maio, M. Basham, F. Yuan, K. Wanelik, *J. Synchrotron Rad.* **2015**, 22(3), 828–838.
- [36] Z. Chen, C. X. Kronawitter, B. E. Koel, *Phys. Chem. Chem. Phys.* **2015**, 17(43), 29387–29393.
- [37] J. D. Hancock, J. H. Sharp, *J. Am. Ceram. Soc.* **1972**, 55, 74–77.
- [38] J. H. Sharp, G. W. Brindley, B. N. N. Achar, *J. Am. Ceram. Soc.* **1966**, 49, 379–382.
- [39] a) M. J. Avrami, *J. Chem. Phys.* **1939**, 7, 1103–1112; b) M. J. Avrami, *J. Chem. Phys.* **1940**, 8, 212–224; c) M. J. Avrami, *J. Chem. Phys.* **1941**, 9, 177–184; d) W. A. Johnson, R. F. Mehl, *Trans. Am. Inst. Min. Metall. Eng.* **1939**, 135, 416–442; e) A. N. Kolmogorov, *Izv. Akad. Nauk SSSR, Ser. Mat; Bull. Acad. Sci. USSR. Ser. Math.* **1937**, 1, 355–359;
- [40] V. G. Hadjiev, M. N. Iliev, I. V. Vergilov, *J. Phys. C: Solid State Phys.* **1988**, 21(7), L199–L201.
- [41] S. Mondini, A. M. Ferretti, A. Puglisi, A. Ponti, *Nanoscale* **2012**, 4(17), 5356–5372.

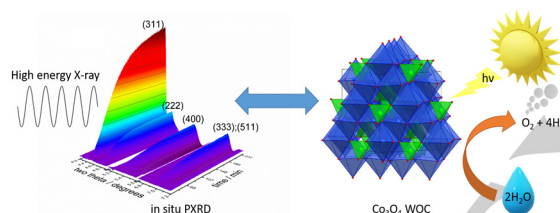
FULL PAPER

- [42] M. Casas-Cabanas, G. Binotto, D. Larcher, A. Lecup, V. Giordani, J.-M. Tarascon, *Chem. Mater.* **2009**, *21*(9), 1939–1947.
- [43] S. R. Gawali, A. C. Gandhi, S. S. Gaikwad, J. Pant, T.-S. Chan, C.-L. Cheng, Y.-R. Ma, S. Y. Wu, *Sci. Rep.* **2018**, *8*(1), 249.
- [44] a) C. A. Charitidis, P. Georgiou, M. A. Koklioti, A.-F. Trompeta, V. Markakis, *Manufacturing Rev.* **2014**, *1*, 11; b) K. Byrappa, M. Yoshimura, *Handbook of hydrothermal technology*; William Andrew, Oxford, **2013**;
- [45] R. I. Walton, F. Millange, D. O'Hare, A. T. Davies, G. Sankar, C. R. A. Catlow, *J. Phys. Chem. B* **2001**, *105*(1), 83–90.
- [46] A. Khorsand Zak, W. H. Abd. Majid, M. E. Abrishami, R. Yousefi, *Solid State Sci.* **2011**, *13*(1), 251–256.
- [47] C.-W. Tang, C.-B. Wang, S.-H. Chien, *Thermochim. Acta* **2008**, *473*(1-2), 68–73.
- [48] R. Xu, H. C. Zeng, *Langmuir* **2004**, *20*(22), 9780–9790.
- [49] J. Xiao, L. Qi, *Nanoscale* **2011**, *3*(4), 1383–1396.
- [50] E. L. Viljoen, M. J. Moloto, Thabede P. M., *DIG. J. Nanomater. Bios.* **2017**, *12*(2), 571–577.
- [51] a) I. Lorite, J. J. Romero, J. F. Fernández, *J. Raman Spectrosc.* **2012**, *43*(10), 1443–1448; b) I. Lorite, J. J. Romero, J. F. Fernandez, *AIP Adv.* **2015**, *5*(3), 37105;
- [52] Z. V. Marinković Stanojević, N. Romčević, B. Stojanović, *J. Eur. Ceram. Soc.* **2007**, *27*(2-3), 903–907.
- [53] X. Hongyan, D. Jiangtao, H. Zhenyin, G. Libo, Z. Qiang, T. Jun, Z. Binzhen, X. Chenyang, *Cryst. Res. Technol.* **2016**, *51*(2), 123–128.
- [54] Z. Nickolov, G. Georgiev, D. Stoilova, I. Ivanov, *J. Mol. Struct.* **1995**, *354*(2), 119–125.
- [55] D. Lin-Vien, N. B. Colthup, W. G. Fateley, J. G. Grasselli, *The Handbook of infrared and raman characteristic frequencies of organic molecules*; Academic Press, Boston, **1991**.
- [56] L. Erdey, F. Paulik, J. Paulik, *Nature* **1954**.
- [57] J. Girardon, A. S. Lermontov, L. Gengembre, P. A. Chernavskii, A. Griboval-Constant, A. Y. Khodakov, *J. Catal.* **2005**, *230*(2), 339–352.
- [58] a) S. Dey, B. Mondal, A. Dey, *Phys. Chem. Chem. Phys.* **2014**, *16*(24), 12221–12227; b) V. M. Jiménez, A. Fernández, J. P. Espinós, A. R. González-Elipe, *J. Electron Spectrosc. Relat. Phenom.* **1995**, *71*(1), 61–71; c) S. C. Petitto, E. M. Marsh, G. A. Carson, M. A. Langell, *J. Mol. Catal. A* **2008**, *281*(1-2), 49–58;
- [59] E. Johansson, L. Nyborg, *Surf. Interface Anal.* **2003**, *35*(4), 375–381.
- [60] a) A. Bergmann, E. Martinez-Moreno, D. Teschner, P. Chernev, M. Gliech, J. F. de Araújo, T. Reier, H. Dau, P. Strasser, *Nat. Commun.* **2015**, *6*, 8625; b) Z. Chen, Z. Duan, Z. Wang, X. Liu, L. Gu, F. Zhang, M. Dupuis, C. Li, *ChemCatChem* **2017**, *9*(19), 3641–3645;
- [61] M. Basham, J. Filik, M. T. Wharmby, P. C. Y. Chang, B. El Kassaby, M. Gerring, J. Aishima, K. Levik, B. C. A. Pulford, I. Sikharulidze, D. Sneddon, M. Webber, S. S. Dhesi, F. Maccherozzi, O. Svensson, S. Brockhauser, G. Nárá, A. W. Ashton, *J. Synchrotron Rad.* **2015**, *22*(3), 853–858.
- [62] F. Song, R. Moré, M. Schilling, G. Smolentsev, N. Azzaroli, T. Fox, S. Lubner, G. R. Patzke, *J. Am. Chem. Soc.* **2017**, *139*(40), 14198–14208.

FULL PAPER

Entry for the Table of Contents

FULL PAPER



New insights into spinel-type Co_3O_4 water oxidation catalyst formation through time-resolved PXRD monitoring using the Oxford-Diamond in situ cell (ODISC) were transferred upon conventional hydrothermal production. This strategy provides key synthesis-activity relationships for optimizing the water oxidation efficiency of Co_3O_4 .

Lukas Reith, Karla Lienau, Daniel S. Cook, René Moré, Richard I. Walton, and Greta R. Patzke*

Page No. – Page No.

Monitoring the hydrothermal growth of cobalt spinel water oxidation catalysts - From preparative history to catalytic activity